Investigation of $CeTi_2O_6$- and $CaZrTi_2O_7$-containing glass-ceramic composite materials

Elham Paknahad and Andrew P. Grosvenor*

Department of Chemistry, University of Saskatchewan, Saskatoon, SK, Canada, S7N 5C9

* Author to whom correspondence should be addressed
E-mail: andrew.grosvenor@usask.ca
Phone: (306) 966-4660
Fax: (306) 966-4730

Abstract

Glass-ceramic composite materials are being investigated for numerous applications (i.e. textile, energy storage, nuclear waste immobilization applications, etc.) due to the chemical durability and flexibility of these materials. Borosilicate and Fe-Al-borosilicate glass-ceramic composites containing brannerite ($CeTi_2O_6$) or zirconolite ($CaZrTi_2O_7$) crystallites were synthesized at different annealing temperatures. The objective of this study was to understand the interaction of brannerite or zirconolite-type crystallites within the glass matrix and to investigate how the local structure of these composite materials changed with changing synthesis conditions. Powder X-ray diffraction (XRD) and Backscattered electron (BSE) microprobe images have been used to study how the ceramic crystallites dispersed in the glass matrix. X-ray absorption near edge spectroscopy (XANES) spectra were also collected from all glass-ceramic composite materials. Examination of Ti K-, Ce L_3-, Zr K-, Si $L_{2,3}$-, Fe K-, and Al $L_{2,3}$-edge XANES spectra from the glass-ceramic composites have shown that the annealing temperature, glass composition, and the loading of the ceramic crystallites in the glass matrix can affect the local environment of the glass-ceramic composite materials. A comparison of the glass-ceramic composites containing brannerite or zirconolite crystallites has shown that similar changes in the long-range and local structure of these composite materials occur when the synthesis conditions to form these materials or the composition are changed.

Keywords: Glass-ceramic composite materials; Nuclear waste immobilization applications; Brannerite; Zirconolite; Borosilicate and Fe-Al-borosilicate glass.

1. Introduction

Glass-ceramic composite materials containing crystalline phases within a glass matrix have received attention for numerous applications in strategic fields such as medicine (bioactive composite as bone replacement and drug delivery systems), photonics, energy storage, aerospace, textiles, and waste management.[1-6] The safe and secure immobilisation of nuclear waste is one of the applications that composite materials have received attention for.[4-10] Extensive studies in the field of nuclear waste sequestration have led to the development of wasteforms based on crystalline ceramics,[11-13] amorphous glasses,[14,15] and glass–ceramic composite materials.[4–6,16] Glass-ceramic composite wasteforms have the potential to provide significantly higher waste loading, enhanced thermal stability, and flexibility compared to glass or ceramic wasteforms alone.[6-10,16-20] For example, radioactive waste elements incorporated in the highly durable crystalline phase within the glass matrix would benefit from a double barrier (ceramic + glass).[4,10,18-20] Studying the local structure of these materials is a crucial step to the development of wasteforms for nuclear waste sequestration.[9,10,17-20]

Borosilicate glasses containing both silicon and boron as network formers were proposed as the first generation wasteform for the immobilisation of high level nuclear waste (HLW) due to the stability and flexibility of the silicate network.[7,14,21,22] It has been suggested that the presence of transition metals (e.g., Fe) in the borosilicate glass can increase the structural stability of these wasteforms.[23-25] The release of β-particles and γ-rays from radioactive elements can lead to the formation of electron-hole pairs in the glass wasteforms and the presence of Fe in the glass has been suggested to be able to trap electron-hole pairs.[23,25] This could result in the materials having an increased resistance to radiation induced structural damage.[23-25]

Titanate ceramics (e.g., SYNROC) are another option for HLW sequestration applications.[26-29] Brannerite, having the composition MTi_2O_6 (M = U, Th, Ce), is one possible host matrix for the immobilization of actinide-bearing radioactive waste.[30-33] The brannerite crystal structure belongs to the monoclinic system, with space group C2/m. The structure consists of alternating columns of edge-sharing MO_6 octahedra with regular shapes and distorted layers of edge-sharing TiO_6 octahedra that are corner sharing with the MO_6 octahedra (Figure 1a).[30,31] Cerium acts as an actinide simulator element in MTi_2O_6 because Ce has a similar ionic radius, coordination environment, and electronic structure to some actinide elements.[31-33] Cerium is not a good simulator element for U because Ce can be easily reduced to Ce^{3+} while U^{3+} is rare; however, Ce is a good simulator element for Pu.[31-33] Moreover, the crystalline structure of brannerite (MTi_2O_6) is a good example for immobilizing uranium-bearing radioactive waste because UTi_2O_6 can hold a significant concentration of uranium (~55 wt% per formula unit).[32,33]

Zirconolite-based ceramics are considered as one of the most promising wasteforms for HLW sequestration applications.[35,36] Previous studies have demonstrated that zirconolite can immobilise both actinides and fission products in the crystal lattice for the long term.[37,38] Zirconolite refers specifically to $CaZrTi_2O_7$, which has a monoclinic structure (space group C2/c). The zirconolite crystal structure forms a monoclinic system that is made up layers of TiO_6 and TiO_5 polyhedra with Ca^{2+} (8 coordinate) and Zr^{4+} (7 coordinate) ions located in the large interstitial sites between these layers (Figure 1b).[39]

The objective of this study is to understand how ceramic crystallites behave within a glass matrix, and to investigate how the local structure of these composite materials change as a result of synthesis conditions. Borosilicate and Fe-Al-borosilicate glass-ceramic composites containing brannerite ($CeTi_2O_6$) or zirconolite ($CaZrTi_2O_7$) crystallites were synthesized at

different annealing temperatures to study the effect of composition and annealing temperature on the local and long-range structure of these materials. Electron microscopy and powder X-ray diffraction (XRD) have been used to study the dispersion of ceramic crystallites in the glass matrix. X-ray absorption near-edge spectroscopy (XANES) was used to investigate changes in the local structure of these materials by collecting Ti K-, Ce L_3-, Zr K-, Si $L_{2,3}$-, Fe K-, and Al $L_{2,3}$- edge XANES spectra.[40]

2. Experimental

2.1. Synthesis

Brannerite was synthesized using the ceramic method. CeO_2 (Alfa Aesar, 99.9%) and TiO_2 (anatase, Alfa Aesar, 99.6%) powders were mixed in stoichiometric amounts, pelleted at 6 MPa and heated in air for six days at 1325 °C with intermediate mixing and pelleting. Zirconolite, nominally $CaZrTi_2O_7$ was also synthesized by the ceramic method using a stoichiometric mixture of CaO, ZrO_2 (Alfa Aesar, 99.7%), and TiO_2 (rutile, Alfa Aesar, 99.9%) powders. Calcium carbonate ($CaCO_3$, ACS, >99%) was heated in air first at 900 °C for one day to decompose to CaO. $CaZrTi_2O_7$ was synthesized by mixing the binary oxides using an agate mortar followed by pressing the mixture into a pellet using a pressure of 6 MPa, and then heating the pellet in air for two days at 1400 °C. The sample was then quench cooled in air, ground, pelleted, and re-heated at 1400 °C for another two days. Diffraction patterns from the ceramics (brannerite and zirconolite) were collected using a PANalytical Empyrean X-ray diffractometer and a Co $K\alpha_{1,2}$ X-ray source at room temperature. Phase analysis was performed using the High Score Plus software package.[41]

Borosilicate glass (BG) and Fe-Al borosilicate glass (FABG) were synthesized by the ceramic method. The compositions of the borosilicate and Fe-Al borosilicate glasses are listed in

Table 1. Appropriate amounts of the respective metal oxide powders were mixed, pressed into pellets at 6 MPa and annealed at 1100 °C for 1 hour in graphite crucibles. Labels used to name the glasses and glass-ceramic composites studied are listed in Table 2.

Glass-ceramic composite materials containing brannerite in borosilicate glass or Fe-Al borosilicate glass (BG/FABG-CeTi$_2$O$_6$) and zirconolite in borosilicate glass or Fe-Al borosilicate glass (BG/FABG-CaZrTi$_2$O$_7$) were synthesized by the ceramic method. The separately synthesized glass and ceramic materials were mixed and then annealed to form glass-ceramic composite materials. Different loadings of CeTi$_2$O$_6$ or CaZrTi$_2$O$_7$ (10 to 40 wt%) were mixed with appropriate amounts of borosilicate glass (BG) or Fe-Al-borosilicate glass (FABG) to form the glass-ceramic composites, pressed into pellets at 6 MPa, and then placed in graphite crucibles. The pellets were heated in air at 1100 or 750 °C for 1 hour. All composite materials were quench cooled in air and were observed to be beads after annealing at 1100 or 750 °C (see Figure 2). It has been reported previously that borosilicate glasses have softening and liquefication points above 800 and 1000 °C, respectively; however, these temperatures can be affected by the glass composition.[21,42,43] The observation of both the glasses and glass-ceramic composites forming beads after annealing at 750 °C indicates that the glass compositions studied here had a liquid state at this temperature. The annealing temperatures used in this study were chosen so as to study how such significant differences in temperature impact the local and long-range structure of the composite materials.

2.2. Electron microprobe analysis

The surface morphologies and chemical compositions of the samples were examined by collecting backscattered electron images (BSE) and energy dispersive X-ray (EDX) maps. BSE images and EDX maps were collected using a JEOL 8600 electron microprobe instrument. The

glass-ceramic composite beads were embedded in a polymer resin and the surfaces of the beads were polished using diamond paste. The samples were coated with carbon to reduce charging effects.[44] BSE images were collected from the composite materials using a magnification of 1000X. Samples were mapped by EDX to determine the chemical composition at different locations.

2.3. XANES

2.3.1. Ti K-, Zr K-, and Ce L$_3$-edges

Ti K-, Ce L$_3$- and Zr K-edge XANES spectra were collected using the Canadian Light Source/X-ray Science Division Collaborative Access Team (CLS@APS, Sector 20) bending magnetic beamline (20BM) located at the Advanced Photon Source (APS), Argonne National Laboratory.[45] A Si (111) double crystal monochromator with a harmonic rejection mirror was used, which provides a photon flux of $\sim 10^{11}$ photons/s.[45] The resolution of the spectra is 0.7 eV at 4966 eV (Ti K-edge), 0.9 eV at 5723 eV (Ce L$_3$-edge), and 2.6 eV at 17998 eV (Zr K-edge).[45] The samples were finely ground and sealed between layers of Kapton tape, and the thickness was adjusted by varying the number of layers of tape to maximize the absorption signal. Multiple scans of each spectrum were collected in fluorescence yield or transmission mode. The transmission spectra were recorded using ionization chambers filled with He$_{(g)}$ and N$_{2(g)}$ to achieve optimal absorption-edge step heights and signal-to-noise ratios.[46] The spectra were also collected in fluorescence mode using a single element vortex silicon detector. XANES spectra were collected using a step size of 0.15 eV/step through the Ti K- and Ce L$_3$-edges and 0.5 eV/step through the Zr K-edge. The Ti K-edge spectra were calibrated using Ti metal (4966 eV) and the Ce L$_3$-edge spectra were calibrated using Cr metal (5989 eV).[33,44] The Zr K-edge spectra

were calibrated using Zr foil as a reference standard with the absorption-edge energy set to 17998.0 eV.[47]

2.3.2. Fe K-edge

The Soft X-ray Microcharacterization Beamline (SXRMB, 06B1-1) located at the Canadian Light Source (CLS) was used to collect the Fe K-edge XANES spectra from Fe-Al borosilicate glass composite materials using a Si (111) monochromator.[48] This beamline provides a photon flux of 10^{11} photons/s and a resolution of 0.7 eV at 7112 eV.[48] The samples were sealed between layers of Kapton tape and the spectra were collected in fluorescence yield and transmission modes using a step size of 0.15 eV through the Fe K-edge. The spectra were calibrated using Fe foil (7112 eV).[48]

2.3.3. Si and Al L$_{2,3}$-edges

The Si and Al L$_{2,3}$-edge XANES spectra were collected from the composite materials using the Variable Line Spacing-Plane Grating Monochromator (VLS-PGM) beamline at the CLS.[49] The samples were prepared by placing ground powder on carbon tape. The spectra were collected in total fluorescence yield (TFY) mode using a step size of 0.05 eV through the Si and Al L$_{2,3}$-edges. The spectra were calibrated using elemental Si for the Si L$_{2,3}$-edge (99.4 eV) and Al metal for the Al L$_{2,3}$-edge (72.5 eV).[44,49] All XANES spectra were normalized and analyzed using the Athena software program.[50]

3. Results and discussion

3.1. Powder X-ray diffraction

Powder XRD patterns from the glass-ceramic composite materials were collected to obtain information about the long-range structure of these materials. The XRD patterns from the glasses (BG and FABG) annealed at different temperatures are shown in Figures 3a and 3b.

Unique powder patterns were observed depending on if the glass-ceramic composite materials were annealed at 750 °C or 1100 °C, as has been observed previously.[44] The patterns from the glasses annealed at 1100 °C (BG-1100 °C and FABG-1100 °C) show only a broad hump which confirms the amorphous structure of these materials. However, the diffraction pattern from the borosilicate glass annealed at 750 °C contains peaks that correspond to the presence of quartz (SiO_2), whereas no such peaks were observed in the XRD pattern from the Fe-Al borosilicate glass annealed at 750 °C. The stabilization of the amorphous structure of the Fe-Al borosilicate glass sample was assumed to be a result of the presence of Al.[44] It was shown previously that Al is responsible for stabilizing the amorphous structure of the Fe-Al-borosilicate glass.[44,51] Aluminum is a network intermediate and can behave as a network former or a network modifier.[8,44,51-53] Al is known to substitute into 4- to 6- coordinate positions, including those normally occupied by Si, and can aid in the formation of the glass.[52-54]

Powder XRD patterns were collected from composite materials containing different amounts of $CeTi_2O_6$ in borosilicate glass annealed at 750 or 1100 °C (Figures 4a and 4b). Diffraction patterns from the BG-$CeTi_2O_6$ composites annealed at 750 °C contain peaks from $CeTi_2O_6$ and quartz, as well as a broad hump that is representative of the amorphous glass matrix. The patterns from the composite materials annealed at 1100 °C (Figures 4b) shows that peaks from brannerite only started to appear in diffraction patterns of the composite materials when 40 wt% of $CeTi_2O_6$ was loaded in the glass matrix. These observations indicate that a significant amount of the brannerite crystallites dissolved in the glass matrix after annealing at 1100 °C.

XRD patterns were also collected from the BG-$CaZrTi_2O_7$ composite materials containing different amounts of $CaZrTi_2O_7$ annealed at 750 or 1100 °C (Figures 5a and 5b).

Examination of the patterns from the composite materials annealed at 1100 °C showed that the minimum loading of $CaZrTi_2O_7$ when peaks representing zirconolite started to appear in the diffraction patterns was 40 wt% (Figure 5b). Diffraction peaks from zirconolite were observed in all patterns from BG-$CaZrTi_2O_7$ annealed at 750 °C regardless of loading (Figure 5a); however, peaks representing the presence of quartz were not observed. The lack of peaks corresponding to the presence of quartz is likely a result of Ca from zirconolite that had dissolved in the glass matrix, acting as a network modifier.[8,37,38,53] These results suggest that a low annealing temperature (i.e., 750 °C) is more favourable to the formation of a composite material with a negligible amount of the ceramic having dissolved in the glass matrix.

XRD patterns from Fe-Al borosilicate glass composite materials containing brannerite or zirconolite annealed at either 750 or 1100 °C are shown in Figures S1 and S2 in the supporting information. Diffraction patterns from these composite materials were observed to be similar to the patterns from borosilicate glass-based composite materials. These results indicate that the type of glass used (i.e., borosilicate or Fe-Al borosilicate) does not influence how the annealing temperature affected the average structure of these composite materials.

3.2. Electron microscopy and EDX

BSE images from the borosilicate glass composite materials (BG-$CeTi_2O_6$/$CaZrTi_2O_7$) annealed at either 750 or 1100 °C are shown in Figure 6. The BSE images from the glass-ceramic composite materials (see Figure 6) show that the brannerite or zirconolite crystallites (bright area) can be differentiated from the glass matrix (dark area). Moreover, air bubbles formed during annealing were also observed in the images from these materials.

The BSE images from the composite materials annealed at 1100 °C (Figures 6b and 6d) contained smaller crystallites when compared to the images from the composite materials

annealed at 750 °C (Figures 6a and 6c). Examination of EDX maps (see Figures S3 and S4 in supporting information) from the composite materials containing brannerite annealed at 1100 °C shows that the glass-like regions contained high concentrations of Ce and Ti (Figure S4). The presence of Ce and Ti was observed only in the ceramic crystallites when an annealing temperature of 750 °C was used to form the glass-ceramic composite materials (Figure S3). These results confirm that more brannerite/zirconolite crystallites dissolved in the glass matrix after annealing at higher temperatures (i.e., 1100 vs 750 °C). These observations are in good agreement with the analysis of the XRD patterns (*vide supra*).

3.3. XANES analysis

Examination of Ti K-, Ce L_3-, Zr K-, Si $L_{2,3}$-, Fe K-, and Al $L_{2,3}$-edge XANES spectra from the glass-ceramic composite materials has allowed for a study of how the annealing temperature, glass composition, and the loading of the ceramic crystallites affected the local environment of the glass-ceramic composites.

3.3.1. Ti K-edge XANES

Ti K-edge XANES spectra were collected from the BG-CeTi$_2$O$_6$ and BG-CaZrTi$_2$O$_7$ composite materials containing 10, 20, and 30 wt% of CeTi$_2$O$_6$ or CaZrTi$_2$O$_7$ annealed at either 750 or 1100 °C (see Figures 7 and 8). Examination of the Ti K-edge spectra shows how the loading of the ceramic (CeTi$_2$O$_6$ or CaZrTi$_2$O$_7$) in the glass matrix and the annealing temperature used can affect the local coordination environment of Ti in the composite materials. These spectra result from 1s$\rightarrow$3d (quadrapolar; pre-edge (A)) and 1s$\rightarrow$4p (dipolar; main-edge (B and C)) transitions.[33,44,55] The pre-edge region (features A_1, A_2 and A_3) contains peaks resulting from local 1s$\rightarrow$3d t_{2g} (A_1) and 1s$\rightarrow$3d e_g^* (A_2) transitions, as well as a third peak (A_3) that results from a non-local, intersite-hybrid excitation involving the transition of 1s electrons to unoccupied 3d

orbitals from a next-nearest-neighbour Ti ion that overlaps with 4p orbitals from the absorbing Ti ion through bridging O 2p orbitals.[33,44,55,56]

The intensity of the pre-edge feature (A) increases while the energy (B) and intensity (C) of the main-edge features decrease with decreasing Ti coordination number (CN).[56-60] The quadrupolar transition (pre-edge (A)) is normally forbidden by dipole selection rules but it becomes allowed with mixing of d and p orbitals.[33,44,56-60] An increase in the intensity of the pre-edge peak is observed for a site without a centre of symmetry (i.e., TiO_4 tetrahedron or a TiO_5 square pyramid) because of the mixing 3d with 4p orbitals, which provides some dipole allowed character to the quadrupolar transition. The pre-edge peak can therefore be used to infer the Ti CN.[33,44,56-60] The energy and intensity of the main-edge features (B and C) can change because of variations in CN and/or oxidation state.[55,61] Feature B can shift to a lower energy because of a decrease in CN.[56-58] A lower CN results in greater final state relaxation effects due to the presence of fewer electrons in the first coordination-shell leading to a shift down in absorption energy.[56] The intensity of feature C is also affected by changes in the CN. As the CN decreases, this reduces the number of Ti 4p-2p O final states available for 1s electrons to be excited to, resulting in a decrease in the intensity of feature C.[56] Feature B (and C) can also shift in energy with changing oxidation state. An increase in the oxidation state will result in fewer electrons being available to screen the nuclear charge and, therefore, more energy is required to excite core electrons leading to an increase in the observed absorption energy.[44,55,61]

Examination of the Ti K-edge spectra from the $BG-CeTi_2O_6$ composite materials annealed at either 750 (Figure 7a) or 1100 °C (Figure 7b) shows that the intensity and energy of the pre-edge and main-edge features changed by varying the loading of brannerite in the glass matrix or by varying the annealing temperature used to form these composite materials. It was

observed that the intensity of the pre-edge feature (A) increased while the energy (B) and intensity (C) of the main-edge features decreased with increasing annealing temperature or decreasing brannerite loading in the composite materials when compared to the spectrum from $CeTi_2O_6$ (see Figures 7a and 7b). These changes in the Ti K-edge XANES spectra were attributed to a decrease in the CN of Ti^{4+}.[56-60] It is recognized that the shift down in energy of feature B could also suggest that Ti^{4+} is reduced in the composite materials, however a reduction in the Ti oxidation should also lead to a decrease in the intensity of the pre-edge peak (feature A) which was not observed. The observed increase in the intensity of feature A and decrease in energy of feature B when comparing the composite materials to $CeTi_2O_6$ can only be attributed to a lowering of the average Ti CN.[33,44,56-60] Titanium adopts a lower CN when incorporated in the glass versus when it is incorporated in brannerite.[44] Moreover, the average Ti CN is lower in the BG-$CeTi_2O_6$ composites annealed at 1100 °C compared to the composites annealed at 750 °C, further confirming that more brannerite dissolved in the glass matrix after annealing at 1100 °C.

Ti K-edge XANES spectra from the BG-$CaZrTi_2O_7$ composite materials annealed at either 750 or 1100 °C are shown in Figures 8a and 8b. The intensity of the pre-edge feature (A) increased with increasing the annealing temperature or decreasing zirconolite loading in the composite materials when compared to the spectrum from $CaZrTi_2O_7$ (see Figures 8a and 8b). These observations indicate that Ti occupies a lower CN when incorporated in the glass than in ceramic.[44] The composite materials containing zirconolite annealed at 1100 °C show a lower Ti CN compared to the composite materials annealed at 750 °C because more zirconolite dissolved in the glass after annealing at 1100 °C. The comparison of the Ti K-edge spectra from the composite materials containing brannerite or zirconolite crystallites show that similar changes in the coordination environment of Ti occur when the synthesis conditions were changed. These

observations show that the local structure of Ti in the glass-ceramic composite materials is affected strongly by the annealing temperature which agree with the powder XRD and electron microscopy results discussed above.

Ti K-edge spectra were also collected from the composite materials containing 30 wt% $CeTi_2O_6$ and 30 wt% $CaZrTi_2O_7$ in Fe-Al borosilicate glass annealed at either 750 or 1100 °C to determine if the type of glass used affects the local coordination environment of Ti in these composite materials (see Figures S5 and S6 in supporting information). Comparing the spectra from the BG-30 wt% $CeTi_2O_6$ and FABG-30 wt% $CeTi_2O_6$ composites annealed at either 750 (Figure S5a) or 1100 °C (Figure S5b) shows that the type of glass used does not affect the behavior of Ti in these glass-ceramic composite materials. Comparison of the spectra from BG and FABG composite materials containing 30 wt% $CaZrTi_2O_7$ annealed at either 750 (Figure S6a) or 1100 °C (Figure S6b) also shows that the behavior of Ti is not affected by changing the type of glass used to form these composite materials.

3.3.2. Ce L_3-edge XANES

Ce L_3-edge XANES spectra were collected from the BG-$CeTi_2O_6$ composite materials annealed at either 750 or 1100 °C to study how the local environment of Ce changes in these materials and are shown in Figure 9. Four features are observed in these spectra from Ce^{4+}, which are labelled as B_1, B_2, B_3, and B_4 (see Fig. 9). The spectra result from a quadrupolar 2p →4f transition (B_1) and three dipolar 2p →5d transitions where the final-states of Ce changes to $4f^2$ (B_2), $4f^1$ (B_3), and $4f^0$ (B_4).[33,62]

Examination of the Ce L_3-edge XANES spectra from the BG-$CeTi_2O_6$ composite materials shows that the intensity and energy of the pre-edge and main-edge features changed when the annealing temperature was changed from 750 to 1100 °C. The observed changes in the

Ce L_3-edge spectra from the composite materials are a result of a variation in the Ce oxidation state.[62,63] The presence of features B_3 and B_4 are indicative of Ce^{4+} while the observation of an intense B_2 peak is indicative of the presence of Ce^{3+}.[33,62,63] Comparing the intensity of features B_2, B_3 and B_4 in the spectra shows that the average Ce oxidation state is lower in the composite materials annealed at 1100 °C versus the composite materials annealed at 750 °C. The changes in the Ce oxidation state can be attributed to a temperature-dependant equilibrium between O and Ce ($2Ce^{4+}+O^{2-} \rightleftharpoons 2Ce^{3+}+O_2$).[33,62,63] As the annealing temperature of the system increases, the equilibrium shifts towards the reduced state of Ce (i.e., Ce^{3+}).[33,62,63] This effect was observed to be much more severe when Ce is contained in the glass matrix than in the ceramic ($CeTi_2O_6$) as a result of brannerite dissolving in the glass matrix when an annealing temperature of 1100 °C was used.[33] The major oxidation state of Ce was observed to be 4+ for all composite materials annealed at 750 °C while the presence of Ce^{3+} increased with decreasing loading of brannerite in the BG-$CeTi_2O_6$ composite materials annealed at 1100 °C. This observation confirms that brannerite dissolved in the glass matrix when the composite materials were annealed at 1100 °C but only up to a certain loading (30-40 wt%) after which some crystalline brannerite was observed to be present.

3.3.3. Zr K-edge XANES

Zr K-edge spectra were collected from the composite materials containing $CaZrTi_2O_7$ in order to understand how the Zr CN in the BG-$CaZrTi_2O_7$ composites was affected by the synthesis conditions used to form these materials (Figure 10). A distinct pre-edge peak (1s→4d) is not observed in the Zr K-edge XANES spectra because of the low resolution of the spectra and the decreased separation between Zr 4d and 5p orbitals when compared to first row transition metals like Ti.[64,65] Although the resolution of the pre-edge peak in the Zr K-edge spectra makes

it difficult to investigate changes in Zr CN, the main-edge features are sensitive to CN changes.[64,65] The spectrum from zirconolite exhibited a broad maximum in the main edge at around 18017 eV, which is in good agreement with previous studies of materials containing 7-coordinate Zr ($Zr^{[7]}$).[64-67] The intensity, energy, and lineshape of the pre-edge and main-edge features of the spectra were observed to change as the annealing temperature of the composite materials was varied. The observed changes in the Zr K-edge XANES spectra (i.e., large differences in the spectral lineshape) have been shown previously to result from variations in the CN of Zr^{4+}.[65-67] A double peak in the main edge with a maximum around 18030 eV is observed in the Zr K-edge XANES spectra from materials containing six-coordinate Zr while a single broad peak in the main edge is observed for materials containing seven-coordinate Zr.[64-67] These observations fit well with the observations of Zr K-edge XANES spectra from the composite materials presented here and indicate that Zr adopts a lower CN when it is incorporated in the glass matrix than in zirconolite crystallites.[68] Moreover, comparing the Zr K-edge XANES spectra from the glass-ceramic composite materials shows that the average Zr CN is lower in the composites annealed at 1100 °C compared to the composite materials annealed at 750 °C. As the annealing temperature increased, the CN of Zr decreased in the composites because of zirconolite crystallites dissolving in the glass matrix.

3.3.4. Si $L_{2,3}$-edge XANES

Si $L_{2,3}$-edge XANES spectra were collected to study how the local structure of Si in the glass was affected by varying the loading of the ceramic, annealing temperature, and the type of glass used to form the composite materials. The Si $L_{2,3}$-edge XANES spectra contain two features that result from 2p→3s (Feature D) and 2p→3d (Feature E) transitions, respectively. The low-energy feature (D) is split into two peaks (D_1 and D_2) due to spin-orbit splitting.[69,70]

It was observed in previous studies of Si $L_{2,3}$ edge XANES spectra that features D and E become narrower to higher energy on going from amorphous silicate to quartz.[44,70-72] The spectra from materials containing amorphous silicates (i.e. glass) have broader peaks to lower energy compared to their crystalline analogues, which can be attributed to the lack of long range order in amorphous silicates.[70-72] As the materials change from amorphous silicates to quartz, a more ordered SiO_4^{4-} tetrahedral bond network would be present, leading to an increase in the degeneracy of Si-O conduction states. This effect results in features D and E becoming narrower to higher energy.[44,70-72]

The Si $L_{2,3}$-edge XANES spectra from the composite materials containing different amounts of $CeTi_2O_6$ or $CaZrTi_2O_7$ in the glass (BG and FABG), and annealed at different temperatures are shown in Figures 11, 12 and S7. The spectra from the corresponding glasses (BG or FABG) are also presented in these figures. The width of the spectral features (D, E) from the composite materials were observed to decrease with increasing loading of the ceramic, decreasing the annealing temperature, or varying the type of glass used to form these materials (i.e., BG vs FABG). The observed changes in the spectra can be attributed to changes in the ordering of the glass in the composites as a result of the partial crystallization of the glass matrix and variations in the glass composition as a result of ceramic crystallites dissolving in the glass network leading to next nearest-neighbour effects between the metal cations and Si.[44,70-73] The next nearest-neighbour metal cation (M) in the Si-O-M bond can influence the strength, length, and bonding characteristics of the Si-O bond.[70-73] The observed changes in the Si $L_{2,3}$ edge XANES spectra from the composite materials indicate that the variation in the loading of $CeTi_2O_6$ or $CaZrTi_2O_7$, the annealing temperature, and the glass composition affect the silicate network. The Si $L_{2,3}$-edge spectra from the BG-composite materials showed more changes when

compared to the spectra from the FABG-composite materials. These observations indicate that the silicate environment in the borosilicate glass matrix is affected to a greater degree than in the Fe-Al borosilicate glass matrix because of the partial crystallization of the borosilicate glass and next nearest-neighbour effects due to the variation in the glass composition.[44] Moreover, the features D and E in the spectra from BG-CeTi$_2$O$_6$-750 °C were observed to be sharper when compared to the spectra from BG-CaZrTi$_2$O$_7$-750 °C. This observation can be attributed to the presence of quartz in the borosilicate glass composite materials containing CeTi$_2$O$_6$ annealed at 750 °C, as quartz was not detected to be present in the BG-CaZrTi$_2$O$_7$-750 °C analogues by XRD.

3.3.5. Fe K-edge XANES

Fe K-edge XANES spectra were collected to study how the redox chemistry of Fe in the Fe-Al borosilicate glass matrix can affect the local structure of the composite materials. The Fe K-edge XANES spectra contain pre-edge (1s→3d, A) and main-edge (1s→4p, B and C) excitations that resemble the features observed in Ti K-edge XANES spectra.[74-76] The Fe K-edge spectra from the composite materials (FABG-30 wt% CeTi$_2$O$_6$ and FABG-30 wt% CaZrTi$_2$O$_7$) annealed at 750 or 1100 °C are shown in Figures 13a and 13b.

The Fe K-edge spectra from the composite materials containing 30 wt% CeTi$_2$O$_6$ or CaZrTi$_2$O$_7$ in Fe-Al borosilicate glass showed a significant shift of the main edge (feature B) to lower energy along with a decrease in the pre-edge peak intensity (feature A) in the composite materials annealed at 1100 °C versus those annealed at 750 °C. The observed decrease in the intensity of feature A and energy of feature B can only be attributed to a variation in Fe oxidation state based on the reasons provided above when discussing the Ti K-edge XANES spectra (section 3.3.1).

The Fe K-edge XANES spectra indicate that the oxidation state of Fe in the composite materials annealed at 1100 °C was reduced to 2+ while the oxidation state of Fe in the composite materials annealed at 750 °C was 3+.[77-79] The observed change in Fe oxidation state with varying annealing temperature is a result of a redox reaction and a temperature-dependant equilibrium between O and Fe ($4Fe^{3+}+2O^{2-} \rightleftharpoons 4Fe^{2+}+O_2$). The equilibrium shifts towards Fe^{2+} when the annealing temperature increases.[44,77-79]

3.3.6. Al L$_{2,3}$-edge XANES

Al L$_{2,3}$-edge XANES spectra were collected from the FABG-CeTi$_2$O$_6$ composite materials annealed at either 750 or 1100 °C to study the local environment of Al (see Figure S8 in supporting information). The spectra contain two features (D and E) that result from 2p→3s and 2p→3d transitions, respectively.[80] It has been shown previously that Al L$_{2,3}$-edge XANES spectra are sensitive to changes in the CN of Al.[80] In the present work, examination of the spectra from the composite materials show negligible changes in the spectral features. These observations indicate that the local structure of Al in the composite materials is not affected considerably by varying the loading of the ceramic or the annealing temperature used to form these composite materials.

4. Conclusions

A good insight into the local structure of glass-ceramic composite materials has been achieved by the investigation of borosilicate and Fe-Al-borosilicate glass-ceramic composites containing brannerite or zirconolite crystallites. These investigations have shown that the CeTi$_2$O$_6$ or CaZrTi$_2$O$_7$ crystallites can dissolve in the glass matrix depending on the ceramic loading, the glass composition, and the annealing temperature used to form these composite materials. It was observed that the CeTi$_2$O$_6$ or CaZrTi$_2$O$_7$ crystallites can dissolve significantly in

the glass matrix when annealed at high temperature. Examination of Ti K- and Zr K-edge XANES spectra from the composite materials indicated that applying a lower annealing temperature is desired for the formation of a composite material with only a small fraction of the ceramic crystallites ($CeTi_2O_6$ or $CaZrTi_2O_7$) having dissolved in the glass matrix. The Si $L_{2,3}$-edge XANES spectra showed that the ordering of the silicate network can be affected depending upon the loading of $CeTi_2O_6$ or $CaZrTi_2O_7$, annealing temperature, and the type of glass used to form these composite materials. Further, the study of the Ce L_3- and Fe K-edge XANES spectra from the Fe-Al-borosilicate composites showed that the oxidation state of Ce and Fe in the glass-ceramic composite materials is strongly affected by the annealing temperature. The comparison of glass-ceramic composite materials containing brannerite and zirconolite has shown that similar changes in the long-range and local structure of these composite materials occurs as a result of changing the synthesis conditions. The study of these composite materials will provide a better understanding of how to develop and design materials as nuclear wasteform materials as well as for other applications.

5. Acknowledgements

6. References

(1) Boccaccini, A. R.; Ferraris, M.; Reece, M. J.; Salvo, M. *Adv. Appl. Ceram.* **2015**, 114, 6753-6761.

(2) El-Meliegy, E.; Noort, R. V. *Glasses and Glass Ceramics for Medical Applications;* Springer Science: New Yourk, USA, 2012.

(3) Wei, X.; Yan, H.; Wang, T.; Hu, Q.; Viola, G.; Grasso, S.; Jiang, Q.; Jin, L.; .Xu, Zh.; Reece, M. J. *J. Appl. Phys.* **2013,** 113, 023510-17.

(4) Digeos, A. A.; Valdez, J. A.; Sickafus, K. E.; Atiq, S.; Grimes, R. W.; Boccaccini, A. R. *J. Mater. Sci.* **2003**, 38, 1597-1604.

(5) Lee, W. E.; Ojovan, M. I.; Stennett, M. C.; Hyatt, N. C. *Adv. Appl. Ceram.* **2006**, 105, 1-12.

(6) Loiseau, P.; Caurant, D. *J. Nucl. Mater.* **2010**, 402, 38-54.

(7) Boccaccini, A. R.; Bernardo, E.; Blain, L.; Boccaccini, D. N. *J. Nucl. Mater.* **2004**, 327, 148-158.

(8) Caurant, D.; Loiseau, P.; Bardez, I.; Gervais, C. *J. Mater. Sci.* **2007**, 42, 8558-8570.

(9) Amoroso, J.; Marra, J. C.; Tang, M.; Lin, Y.; Chen, F.; Su, D.; Brinkman, K. S. *J. Nucl. Mater.* **2014**, 454, 12-21.

(10) Zhang, Y.; Zhang, Z.; Thorogood, G.; Vance, E. R. *J. Nucl. Mater.* **2013**, 432, 545-547.

(11) Ewing, R. C. *Can. Mineral.* **2005**, 43, 2099-2116.

(12) Laverov, N. P.; Yudintsev, S. V.; Livshits, T. S.; Stefanovsky, S. V.; Lukinykh, A. N.; Ewing, R. C. *J. Geochemistry International.* **2010**, 48, 1-14.

(13) Lian, J.; Wang, L. M.; Lumpkin, G. R.; Ewing. R. C. *Nuclear Instruments and Methods in Physics Research B*. **2002**, 191, 565-570.

(14) Raj, K.; Kaushik, C. P. *Materials Science and Engineering*. **2009**, 2, 1-6.

(15) Ojovan, M. I.; Lee, W. E. *Metallurgical and Materials Transactions.* **2011**, 42, 837-851.

(16) Ojovan, M. I.; Juoi, J. M.; Lee, W. E. *J Pak Mater Soc*. **2008**, 2, 72-76.

(17) Martin, C.; Ribet, I.; Frugier, P.; Gin, S. *J. Nucl. Mater.* **2007**, *366*, 277–287.

(18) Ewing, R. C.; Webert, W. J.; Clinard, F. W. *Prog. Nucl. Energy*. **1995**, 29, 63-121.

(19) Pace, S.; Cannillo, V.; Wu, J.; Boccaccini, D. N.; Seglem, S.; Boccaccini, A. R. *J. Nucl. Mater.* **2005**, 341, 12-18.

(20) Boccaccini, A. R.; Afiq, S.; Grimes, R. W. *Adv. Eng. Mater.* **2003**, 5, 501-508.

(21) Marples, J. A. C. *Glass Technol*. **1988**, 29, 230.

(22) Ojovan, M. I.; Lee, W. E. *An Introduction to Nuclear Waste Immobilization*; Elsevier: Amsterdam, 2005.

(23) McGann, O. J.; Bingham, P. A.; Hand, R. J.; Gandy, A. S.; Kavcic, M.; Itnik, M. Z.; Bucar, K.; Edge, R.; Hyatt, N. C. *J. Nucl. Mater.* **2012**, 429, 353-367.

(24) Malchukova, E.; Boizot, B.; Petite, G.; Ghaleb, D. *Eur. Phys. J. Appl. Phys.* **2009**, 45, 10701-10710.

(25) McGann, O. J.; Gandy, A. S.; Bingham, P. A.; Hand, R. J.; Hyatt, N. C. *MRS Proc.* **2013**, 1518, 41-46.

(26) Lutze, W.; Ewing, R. C. *Radioactive Waste Forms for the Future;* Elsevier: Amsterdam, 1988.

(27) Ringwood, A. E.; Oversby, V. M.; Kesson, E. S.; Sinclair, W.; Ware, N.; Hibberson, W. *Nucl. Chem. Waste Manage.* **1981**, 2, 287-305.

(28) Ringwood, A. E.; Kesson, E. S.; Ware, N. G.; Hibberson, W. *Nature.* **1979**, 278, 219-223.

(29) Sickafus, K. E.; Grimes, R. W.; Valdez, J. A.; Cleave, A.; Tang, M.; Ishimaru, M.; Corish, S.; Stanek, C. R.; Uberuaga, B. P. *Nature Mater.* **2007**, 6, 217-223.

(30) Lumpkin, G. R.; Smith, K. L.; Blackford, M. G. *J. Nucl. Mater*. **2001**, 289, 177-187.

(31) Helean, K. B.; Navrotsky, A.; Lumpkin, G. R.; Colella, M.; Lian, J.; Ewing, R. C.; Ebbinghaus, B.; Catalano, J. G. *J. Nucl. Mater*. **2003**, 320, 231-244.

(32) Lopez, C.; Deschanels, X.; Bart, J. M.; Boubals, J. M.; Den Auwer, C.; Simoni, E. *J. Nucl. Mater*. **2003**, 312, 76-80.

(33) Huynh, L. T.; Eger, Sh. B.; Walker, J. D. S.; Hayes, J. R.; Gaultois, M. W.; Grosvenor, A. P. *Solid State Sciences*. **2012**, 14, 761-767.

(34) Momma K.; Izumi, F. *J. Appl. Crystallogr.* **2008**, 41, 653-658.

(35) Stefanovsky, S. V.; Nikokov, B. S.; Omelianenko, B. I.; Yudintsev, S. V.; Yakushev, A. I. *Phys. Chem. Mat. Treat*. **1997**, 111-117.

(36) Yudintsev, S. V.; Omelianenko, B. I.; Stefanovsky, S. V.; Ochkin, A. V.; Chizhevskaya, S. V. *J. Adv. Mat*. **1998**, 91-100.

(37) Caurant, D.; Loiseau, P.; Bardez, I. *Journal of Nuclear Materials*. **2010**, 407, 88-99.

(38) Zhang, Y.; Stewart, M. W. A.; Li, H.; Carter, M. L.; Vance, E. R.; Moricca, S. *J. Nucl. Mater*. **2009**, 395, 69-74.

(39) Salamat, A.; McMillan, P. F.; Firth, S.; Woodhead, K.; Hector, A. L.; Garbarino, G.; Stennett, M. C.; Hyatt, N. C. *J. Inorg. Chem*. **2013**, 52, 1550-1558.

(40) De Groot, F. M. F. *Chem. Rev.* **2001**, 101, 1779-1808.

(41) PANalytical B. V. X'Pert HighScore Plus.Version 3.0; Almelo: Netherlands, 2011.

(42) Wallenberger, F. T.; Watson, J. C.; Li, H. *ASM: Composites*, **2001**, 21, 27-34.

(43) Hrma, P.; Schweiger, M. J.; Humrickhouse, C. J.; Moody, J. A.; Tate, R. T.; Rainsdon, T. T.; TeGrotenhuis, N. E.; Arrigoni, B. M.; Marcial, J.; Rodriguez, C. P.; Tincher, B. H. *Ceramics – Silikáty*, **2010**, 54, 193-211.

(44) Aluri E. R.; Grosvenor, A. P. *RSC Adv.* **2015**, 5, 10477-10486.

(45) Heald, S. M.; Brewe, D. L.; Stern, E. A.; Kim, K. H.; Brown, F. C.; Jiang, D. T.; Crozier, E. D.; Gordon, R. A. *J. Synchrotron Rad.* **1999**, 6, 347-349.

(46) Aluri, E. R.; Hayes, J. R.; Walker, J. D. S.; Grosvenor, A. P. *J. Phys. Chem. C.* **2014**, 15, 7910-7922.

(47) Thompson, A.; Attwood, D.; Gullikson, E.; Howells, M.; Kim, K. J.; Kirz, J.; Kortright, J.; Lindau, I.; Yanwei, L.; Pianetta, P.; Robinson, A.; Scofield, J.; Underwood, J.; Williams, G.; Winick, H. *X-ray Data Booklet*; Lawrence Berkeley National Laboratory: Berkeley, CA, 2001.

(48) Hu, Y. F.; Coulthard, I.; Chevrier, D.; Wright, G.; Igarashi, R.; Sitnikov, A.; Yates, B. W.; Hallin, E. L; Sham, T. K.; Reininger, R.; Garrett, R.; Gentle, I.; Nugent, K.; Wilkins, S. *AIP Conf. Proc.* **2009**, 1234, 343-346.

(49) Hu, Y. F.; Zuin, L.; Reininger, R.; Sham, T. K. *AIP Conf. Proc.* **2007**, 879, 535-538.

(50) Ravel, B.; Newville, M. *J. Synchrotron Rad.* **2005**, 12, 537-541.

(51) Singh, J.; Singh, D.; Singh, S. P.; Mudahar, G. S.; Thind, K. S. *Mater. Phys. Mech.* **2014**, 19, 9-15.

(52) Sen, S.; Youngman, R. E. *J. Phys. Chem. B.* **2004**, 108, 7557-7564.

(53) Zachariasen, W. H. *J. Am. Chem. Soc.* **1932**, 54, 3841–3850.

(54) Zheng, Q. J.; Youngman, R. E.; Hogue, C. L.; Mauro, J. C.; Potuzak, M.; Smedskjaer, M. M.; Yue, Y. Z. *Phys. Rev. B.* **2012**, 86, 1-12.

(55) Cabaret, D.; Joly, Y.; Renevier, H.; Natoli, C. R. *J. Synchrotron Rad.* **1999**, 6, 258-260.

(56) Gaultois, M. W.; Grosvenor, A. P. *J. Mater. Chem.* **2011**, 21, 1829-1836.

(57) Farges, F.; Brown, G. E.; Rehr, J. J. *Phys. Rev. B.* **1997**, 56, 1809-1819.

(58) Farges, F. *Am. Mineral.* **1997**, 82, 44-50.

(59) Joly, Y.; Cabaret, D.; Renevier, H.; Natoli, C. R. *Phys. Rev. Lett.* **1999**, 82, 2398-2401.

(60) Romano, C.; Paris, E.; Poe, B. T.; Giuli, G.; Dingwell, D. B.; Mottanai, A. *American Mineralogist.* **2000**, 85, 108-117.

(61) Greaves, G. N.; Barrett, N. T.; Antonini, G. M.; Thornley, F. R.; Willis, B. T. M.; Steel, A. *Am. Chem. Soc.* **1989**, 111, 4313-4324.

(62) Kotani, A.; Kvashnina, K.O.; Butorin, S.M.; Glatzel, P. *J. Electron. Spectrosc. Rel. Phenom.* **2001**, 184, 210-215.

(63) Lopez, C.; Deschanels, X.; Bart, J. M.; Boubals, J. M.; Den Auwer, C.; Simoni, E. *J. Nucl. Mater.* **2003**, 312, 76-80.

(64) Mountjoy, G.; Anderson, R.; Newport, R. J.; Smith, M. E. *J. Condens. Matter.* **2000**, 12, 3505-3519.

(65) Gaultois, M. W.; Greedan, J. E.; Grosvenor, A. P. *J. Electron Spectroscopy and Related Phenomena.* **2011**, 184, 192-195.

(66) Mountjoy, G.; Pickup, D. M.; Anderson, R.; Wallidge, G. W.; Holland, M. A.; Newport, R. J.; Smith, M. E. *J. Phys. Chem. Chem. Phys.* **2000**, 2, 2455-2460.

(67) Jollivet, P.; Calas, G.; Galoisy, L.; Angeli, F.; Bergeron, B.; Gin, S.; Ruffoni, M. P.; Trcera, N. *Journal of Non-Crystalline Solids.* **2013**, 381, 40-47.

(68) Patzig, C.; Höche, T.; Hu, Y.; Ikeno, H.; Krause, M.; Dittmer, M.; Gawronski, A.; Rüssel, C.; Tanaka, I.; Henderson, G. S. *Journal of Non-Crystalline Solids.* **2014***, 384, 47-54.

(69) Li, D.; Bancroft, G. M.; Kasrai, M.; Fleet, M. E.; Feng, X. H.; Tan, K. H.; Yang, B. X. *Solid State Commun.* **1993**, 87, 613-617.

(70) Li, D.; Bancroft, G. M.; Kasrai, M.; Fleet, M. E.; Secco, R. A.; Feng, X. H.; Tan, K. H.; Yang B. X. *Am. Mineral*. **1994**, 79, 622-632.

(71) Garvie, L. A. J.; Buseck, P. R. *Am. Mineral.* **1999**, 84, 946-964.

(72) Harp, G. R.; Saldin, D. K.; Tonner, B. P. *J. Condens. Matter.* **1993**, 5, 5377-5388.

(73) Sammynaiken, R.; Naftel, S. J.; Sham, T. K.; Cheah, K. W.; Averboukh, B.; Huber, R. *Journal of applied physics*. **2002**, 92, 3000-3006.

(74) Hayes J. R.; Grosvenor, A. P. *J. Alloys Comp.* **2012**, 537, 323-331.

 (75) Sigrist, J. A.; Gaultois M. W.; Grosvenor, A. P. *J. Phys. Chem. A*. **2011**, 115, 1908-1912.

(76) Westre, T. E.; Kennepohl, P.; Dewitt, J. G.; Hedman, B.; Hodgson K. O.; Solomon, E. I. *J. Am. Chem. Soc.* **1997**, 119, 6297-6314.

(77) Magnien, V.; Neuville, D. R.; Cormier, L.; Roux, J.; Hazemann, J. L.; Pinet, O.; Richet, P. *J. Nucl. Mater.* **2006**, 352, 190-195.

(78) Mehdikhani, B.; Borhani, G. H. *Process. Appl. Ceram.* **2013**, 7, 117-121.

(79) Vickridge, I.; Pinet, O.; Richet, P. *Geo. Cosmo. Acta.* **2008**, 72, 2157-2168.

(80) Walker, J. D. S.; Grosvenor, A. P. *Inorg. Chem.* **2013**, 52, 8612-8620.

Tables

Table 1: Compositions of the synthesized glasses.

Glass	SiO$_2$ (mol %)	B$_2$O$_3$ (mol %)	Na$_2$O (mol %)	CaO (mol %)	Fe$_2$O$_3$ (mol %)	Al$_2$O$_3$ (mol %)
Borosilicate (BG)	63.5	16.9	16.5	3.1	-	-
Fe-Al borosilicate (FABG)	55.5	16.9	16.5	3.1	3.0	5.0

Table 2: Labels used to name the glasses and glass-ceramic composites studied.

Label	Sample description
BG	Borosilicate glass
FABG	Fe-Al-borosilicate glass
BG-CeTi$_2$O$_6$-750/1100 ºC	Composite materials containing brannerite in borosilicate glass annealed at either 750 or 1100 ºC
BG-CaZrTi$_2$O$_7$-750/1100 ºC	Composite materials containing zirconolite in borosilicate glass annealed at either 750 or 1100 ºC
BG-XX wt% CeTi$_2$O$_6$ or CaZrTi$_2$O$_7$	Composite materials containing XX wt% brannerite or zirconolite in borosilicate glass
FABG-XX wt% CeTi$_2$O$_6$ or CaZrTi$_2$O$_7$	Composite materials containing XX wt% brannerite or zirconolite in Fe-Al borosilicate glass

Figure Captions

Figure 1: The monoclinic crystal structures of (a) $CeTi_2O_6$ and (b) $CaZrTi_2O_7$ are shown. The structures were generated using the VESTA program.[34]

Figure 2: Photographs of the composite material containing 30 wt% $CeTi_2O_6$ in borosilicate glass after annealing at (a) 750 or (b) 1100 °C are shown.

Figure 3: XRD patterns from (a) borosilicate glass annealed at 750 or 1100 °C and (b) Fe-Al borosilicate glass annealed at 750 or 1100 °C are shown. Diffraction peaks from quartz are marked by an asterisk (*).

Figure 4: XRD patterns from the composite materials containing 10, 20, 30 and 40 wt% loading of $CeTi_2O_6$ in borosilicate glass annealed at (a) 750 or (b) 1100 °C are shown. Diffraction peaks from quartz are marked by an asterisk (*).

Figure 5: XRD patterns from the composite materials containing 10, 20, 30 and 40 wt% loading of $CaZrTi_2O_7$ in borosilicate glass annealed at (a) 750 or (b) 1100 °C are shown.

Figure 6: Backscattered images from (a) BG-30 wt% $CeTi_2O_6$-750 °C, (b) BG-30 wt% $CeTi_2O_6$-1100 °C, (c) BG-30 wt% $CaZrTi_2O_7$-750 °C, and (d) BG-30 wt% $CaZrTi_2O_7$-1100 °C are shown. The scale bar in each image is 10 μm.
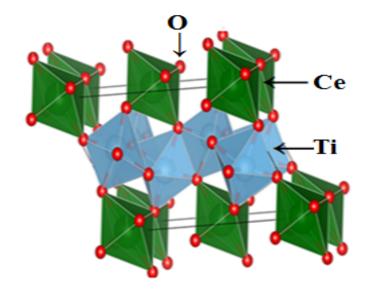
Figure 7: Ti K-edge XANES spectra from (a) BG-$CeTi_2O_6$-750 °C and (b) BG-$CeTi_2O_6$-1100 °C containing 10, 20 and 30 wt% loading of $CeTi_2O_6$ are shown. The spectrum from $CeTi_2O_6$ is also presented. Feature A represents the pre-edge region (1s→3d) and is shown in the inset. Features B and C (1s→4p) represent the main-edge region. The arrows show how the intensity or energy of the spectral features change with decreasing loading of the ceramic in the glass-ceramic composites when compared to the spectrum from $CeTi_2O_6$.

Figure 8: Ti K-edge XANES spectra from (a) BG-CaZrTi$_2$O$_7$-750 $^\circ$C and (b) BG-CaZrTi$_2$O$_7$-1100 $^\circ$C containing 10, 20 and 30 wt% loading of CaZrTi$_2$O$_7$. The spectrum from CaZrTi$_2$O$_7$ is also presented. Feature A (pre-edge region) is shown in the inset. The arrows show how the intensity of the pre-edge feature (A) increased with decreasing loading of the ceramic in the glass-ceramic composites when compared to the spectrum from CaZrTi$_2$O$_7$.

Figure 9: Ce L$_3$-edge XANES spectra from BG-CeTi$_2$O$_6$ composite materials containing 10, 20 and 30 wt% loading of CeTi$_2$O$_6$ annealed at 750 or 1100 $^\circ$C are shown.

Figure 10: Zr K-edge XANES spectra from BG-CaZrTi$_2$O$_7$ composite materials containing 10, 20 and 30 wt% loading of CaZrTi$_2$O$_7$ annealed at 750 or 1100 $^\circ$C are shown. The spectrum from CaZrTi$_2$O$_7$ is also presented for comparison.

Figure 11: Si L$_{2,3}$-edge XANES spectra from (a) BG-CeTi$_2$O$_6$-750 $^\circ$C and (b) FABG-CeTi$_2$O$_6$-750 $^\circ$C containing 10, 20 and 30 wt% loading of CeTi$_2$O$_6$ are shown. The spectra are compared to the spectrum from the corresponding glass (BG or FABG).

Figure 12: Si L$_{2,3}$-edge XANES spectra from (a) BG-CaZrTi$_2$O$_7$-750 $^\circ$C and (b) FABG-CaZrTi$_2$O$_7$- 750 $^\circ$C containing 10, 20 and 30 wt% loading of CaZrTi$_2$O$_7$ are shown. The spectra are compared to the spectrum from the corresponding glass (BG or FABG).

Figure 13: Fe K-edge XANES spectra from (a) FABG-30 wt% CeTi$_2$O$_6$ -750 or 1100 $^\circ$C, and (b) FABG-30 wt% CaZrTi$_2$O$_7$-750 or 1100 $^\circ$C. The spectra result from 1s$\rightarrow$3d (feature A) and 1s$\rightarrow$4p (Features B and C) transitions, respectively. The arrows show a shift of the main edge (feature B) to lower energy along with a decrease in the pre-edge peak intensity (feature A) in the composite materials annealed at 1100 $^\circ$C versus those annealed at 750 $^\circ$C.
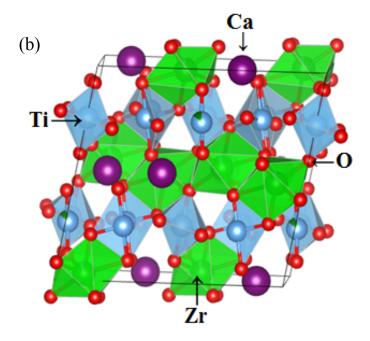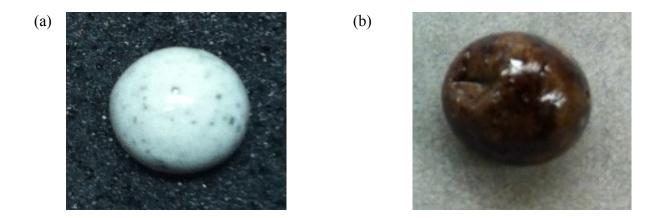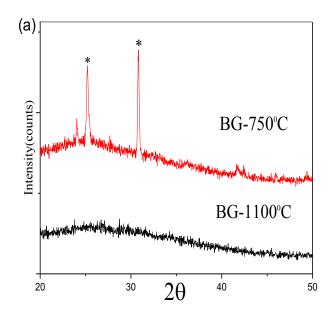
Figure 1:

(a)

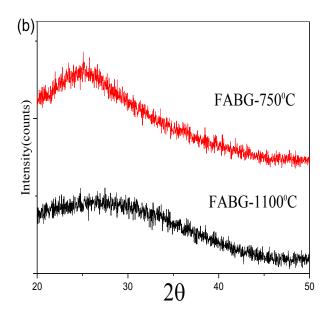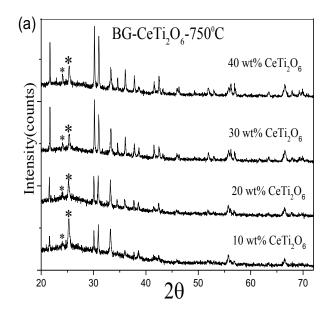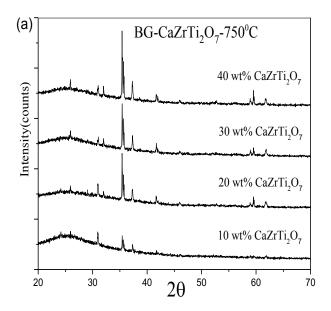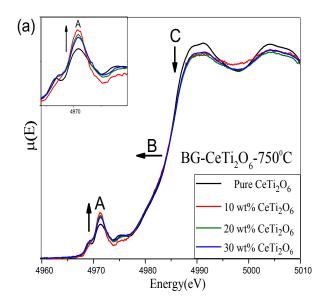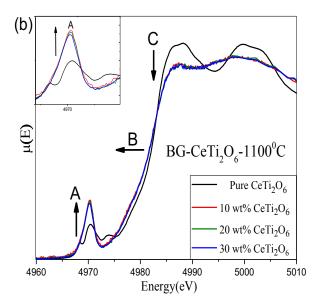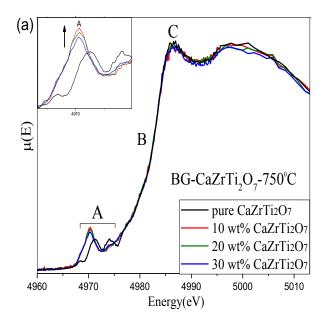(b)

Figure 2:

(a)

(b)

Figure 3:

Figure 4:

Figure 5:

(a) BG-CaZrTi$_2$O$_7$-750^{0}C with traces labeled 40 wt% CaZrTi$_2$O$_7$, 30 wt% CaZrTi$_2$O$_7$, 20 wt% CaZrTi$_2$O$_7$, 10 wt% CaZrTi$_2$O$_7$

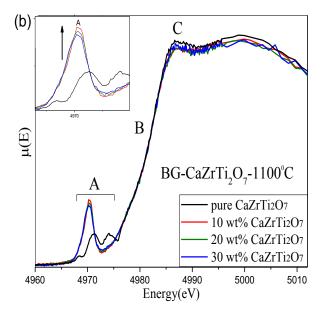(b) BG-CaZrTi$_2$O$_7$-1100^{0}C with traces labeled 40 wt% CaZrTi$_2$O$_7$, 30 wt% CaZrTi$_2$O$_7$, 20 wt% CaZrTi$_2$O$_7$, 10 wt% CaZrTi$_2$O$_7$

Figure 6:

Figure 7:

Figure 8:

(a)

C

B

$BG\text{-}CaZrTi_2O_7\text{-}750^0C$

A

μ(E)

— pure CaZrTi2O7
— 10 wt% CaZrTi2O7
— 20 wt% CaZrTi2O7
— 30 wt% CaZrTi2O7

4960   4970   4980   4990   5000   5010
Energy(eV)

(b)

C

B

$BG\text{-}CaZrTi_2O_7\text{-}1100^0C$

A

μ(E)

— pure CaZrTi2O7
— 10 wt% CaZrTi2O7
— 20 wt% CaZrTi2O7
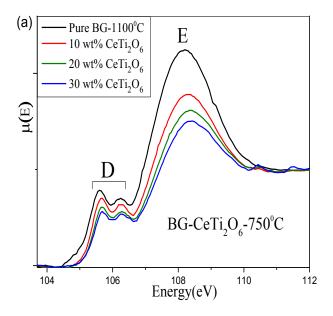— 30 wt% CaZrTi2O7

4960   4970   4980   4990   5000   5010
Energy(eV)

Figure 9:

Figure 10:

Figure 11:

Figure 12:

Figure 13:

(a)

C

B

μ(E)

A

—— FABG-30 wt% CeTi$_2$O$_6$-1100^{0}C

—— FABG-30 wt% CeTi$_2$O$_6$-750^{0}C

7120   7140   7160   7180

Energy(eV)

(b)

C

B

μ(E)

A

—— FABG-30 wt% CaZrTi$_2$O$_7$-1100^{0}C

—— FABG-30 wt% CaZrTi$_2$O$_7$-750^{0}C

7120   7140   7160   7180

Energy(eV)